Supporting Information for

Solvent Gaming Chemistry to Control the Quality of Halide Perovskite Thin Films for Photovoltaics

Xiaofeng Huang,[1†] Guocheng Deng,[1†] Shaoqi Zhan,[2,†] Fang Cao,[1] Fangwen Cheng,[1] Jun Yin,[1,3] Jing Li,[1,3] Binghui Wu,[1,3,*] Nanfeng Zheng[1,3,*]

[1] State Key Laboratory for Physical Chemistry of Solid Surfaces, Collaborative Innovation Center of Chemistry for Energy Materials, National & Local Joint Engineering Research Center of Preparation Technology of Nanomaterials, College of Chemistry and Chemical Engineering, Pen-Tung Sah Institute of Micro-Nano Science and Technology, Xiamen University, Xiamen 361005, China.

[2] Department of Chemistry-BMC, Uppsala University, BMC Box 576, S-751 23 Uppsala, Sweden.

[3] Innovation Laboratory for Sciences and Technologies of Energy Materials of Fujian Province (IKKEM), Xiamen 361102, China

[†]These authors contributed equally to this work.

*Corresponding authors. Emails: binghuiwu@xmu.edu.cn (B.W.); nfzheng@xmu.edu.cn (N.Z.).

Methods

Precursor materials. All chemicals and reagents were used without any further purification. Lead iodide (PbI_2) and Cesium iodide (CsI) were purchased from TCI (Tokyo Chemical Industry Co., Ltd.); Formamidinium iodide (FAI) from Greatcell. Lead chloride ($PbCl_2$), phenylethylamine iodide (PEAI), 4-tert-butylpyridine (tBP), lithium bis (trifluoromethanesulfonyl) imide (Li-TFSI) and 2,2',7,7-tetrakis (*N*,*N*-di-p-methoxyphenylamine)-9,9'-spirobifluorene (Spiro-OMeTAD) from Xi'an Polymer Light Technology Corp.; 4-Fluorophenol and 4-Fluoroanisole from Aladdin; 2-methoxyethanol (2ME) and all other solvents from Sinopharm Chemical Regent Co., Ltd.

Growth of Crystals. PbI_2-OXR: 461 mg of PbI_2 powders (or 172 mg of FAI and 461 mg of PbI_2 powders, or 633 mg of $FAPbI_3$ powders) were dissolved by solvents such as DMSO (dimethyl sulfoxide), DMPU (*N*,*N*-dimethylpropyleneurea) or DESO (diethyl sulfoxide) under 100 ^oC heating and stirring. Then ethyl acetate, chlorobenzene or chloroform was slowly diffused into these filtered solutions in a closed container at room temperature. After two or three days, the crystals crystallized from above solutions. CCDC numbers: 2104894, (PbI_2-2DESO); 2104895, (PbI_2-DMPU); 2104896, (PbI_2-2DMSO).

(FA···OXR)PbI_3: 172 mg of FAI and 461 mg of PbI_2 powders (or 633 mg of $FAPbI_3$ powders) were dissolved by solvents such as DMF (*N*,*N*-dimethylformamide), PDI (2-pyrrolidinone), TMSO (tetramethylene sulfoxide), NMP (*N*-methylpyrrolidone), DMI (1,3-dimethyl-2-imidazolidinone), DMA (*N*,*N*-dimethylacetamide), HMPA (hexamethyl phosphoryl triamide) or TPPO (tris(*N*,*N*-tetramethylene)phosphoric acid triamide) under 100 ^oC heating and stirring. Then ethyl acetate, chlorobenzene or chloroform was slowly diffused into these filtered solutions in a closed container at room temperature. After two to three days, the crystals crystallized from above solutions. CCDC numbers: 2104889, [(FA···0.5DMA)PbI_3]; 2104890, [(FA···2DMF)PbI_3]; 2104891, [(FA···2.5DMI)PbI_3]; 2104892, [(FA···HMPA)PbI_3]; 2104893, [(FA···NMP)PbI_3].

Precursor preparation. Precursor preparation of perovskite layers. 729 mg of (FA···NMP)PbI_3, or 603 mg of PbI_2-2DMSO and 172 mg of FAI powders were dispersed by 600 μL of 2ME solvent to obtain clear precursors. For additive-contained precursor, 60 μL of CsI/2ME solution (130 mg/mL) and 2.78 mg of $PbCl_2$ were added into above precursors before using.

Solution preparation of hole-transition layers. The Spiro-OMeTAD/chlorobenzene (72 mg/mL) solution was doped with the additives containing 17.5 μL of Li-TFSI/ACN (520 mg/mL) and 28.8

μL of tBP. The synthetic nickel phthalocyanine powders were dissolved by chloroform (10 mg/mL) without any additives.

Solar cell and module fabrication. FTO glasses (NSG, 7 Ω per square) in sizes of 2 × 2 cm^2 or 6 × 6 cm^2 were ultrasonically cleaned with distilled water, acetone, and 2-propanol. After drying with N_2, the substrate was treated with ozone for 15 min and a compact $ZnTiO_3$ layer was deposited by spray pyrolysis at 450 °C.[1] After cooling to room temperature, an ethanol solution (1 M) of thiourea was span coating on the above $ZnTiO_3$ substrate at 3000 rpm for 30 s, followed by 450 °C heating for 30 min. A 150 nm-thickness mesoporous TiO_2 film was deposited on the as-prepared $ZnTiO_3$ substrate with ethanol solution (1:5, mass ratio) of TiO_2 paste (Dyesol DSL 18NR-T), which was followed by heating at 450 °C for 60 min. The preparation of perovskite film was conducted as following: a dose of perovskite precursor (typically 3 μL for 2 × 2 cm^2 substrate and 30 μL for 6 × 6 cm^2) was dipped into the gap (~200 μm) between the blade and as-prepared substrate, followed by the automatically moving at a speed of ~1000 $mm\cdot s^{-1}$. Then the wet thin film was quickly transferred into a homemade vacuum chamber to undergo the vacuum-flash process, which could be pumped to ~10^1 Pa within 10 s, and then the as-prepared substrate was annealed at different temperatures for 30 min. After preparation of the perovskite layer, a PEAI/2-propanol solution (3 mg/mL) was span onto the perovskite film at 5000 rpm for 30 s. Then the hole transport layer solution was coated dynamically at 3000 rpm for 30 s. Finally, 80 nm-thickness Au counter electrode was deposited by thermal evaporation under a reduced pressure of 2 × 10^{-7} Torr. All the above processes were manufactured in ambient air at ~30% RH.

Module fabrication. To fabricate the perovskite solar modules, the FTO electrode / $ZnTiO_3$ / Perovskite / HTL / Au electrode layers were laser-scribed sequentially to form a P1-P4-P2-P3 pattern as shown in Figure S19b. The active area of small-scale device and large-scale module were 0.12 cm^2 and 18 cm^2, respectively.

Module encapsulation. The redundant edge of perovskite film was etched by laser scribe firstly. Encapsulant PIB (polyisobutylene) and glass were successively put onto the module at N_2 atmosphere, then the as-prepared sample was transferred to a hot-press machine for combination of module and glass, the process was maintained at 100 °C for 5 min.

Characterizations. The diffraction data of PbI_2-OXR and (FA···OXR) PbI_3 crystals were collected on an Agilent Technologies SuperNova system and the data were processed using CrysAlis. The structure was solved and refined using full-matrix least-squares based on F^2 with program SHELXS-97 and SHELXL-97 within Olex2. Raman spectra were recorded on a Confocal *in-situ* Raman Spectroscope. ^{1}H NMR and *in-situ* ^{1}H NMR spectra were recorded on a AVANCE NEO 500 MHz Digital FT-NMR Spectrometer. TG and DSC data were collected by 449F5 and DSC214 from NETZSCH-Gerätebau GmbHand, respectively. Surface morphologies and surface potentials were recorded on a SEM-4800 field-mission scanning electron microscope and Oxford Instruments Asylum Research Cypher ES, respectively. XRD patterns were analyzed on an X-ray diffractometer (Rigaku, RINT-2500) with a Cu Kα radiation source. XPS data were measured by Thermo Scientific ESCALAB Xi$^+$. The time-resolved photoluminescence spectra were measured on an Edinburgh Instruments FLS980 spectrometer, and the data were fitted with biexponential functions τ = A + B$_1$ exp(−t/τ$_1$) + B$_2$ exp(-t/τ$_2$). For Mott-Schottky analysis, capacitance-voltage measurements were performed at fixed frequency (1 kHz) and the calculation formula was $1/C^2 = 2/[(e\varepsilon\varepsilon_0 N)(V\text{-}V_{\mathrm{bi}}\text{-}(\mathrm{k_B}T)/e)]$, where e is the elementary charge, ε is the dielectric constant of perovskite, ε_0 is the permittivity of vacuum, N is the carrier density, V_{bi} is the flat band potential, $\mathrm{k_B}$ is the Boltzmann constant and T is the absolute temperature. Current-voltage characterizations were recorded on a solar simulator equipped with a Keithley 2400 source meter and a 300-W collimated xenon lamp (Newport) calibrated with a light intensity to 100 mW cm^{-2} at AM 1.5 G solar light. The dark current density of devices was recorded on the same Keithley 2400 Source Meter in dark condition. IPCE values were measured on a computer-controlled IPCE system (Newport) containing a xenon lamp, a monochromator, and a Keithley multimeter and collected at DC mode. The stabilized power output of the PSCs/modules was measured using the Keithley 2400 source meter under AM 1.5 simulated solar irradiation, and a bias at the corresponding maximum power point (MPP) was applied.

DFT calculation. All the DFT calculations were performed by the Vienna ab initio simulation package (VASP).[2,3] The electron-core interactions were described by the projected augmented wave (PAW)[4] method and electron exchange–correlation was expressed at the general gradient-approximation (GGA) level by the Perdew–Burke–Ernzerhof (PBE) functional.[5] A cutoff energy of 500 eV was adopted for the plane-wave basis set. All calculations were performed with spin polarization. For structural optimization, a convergence threshold of 0.02 eV Å^{-1} was set in force and the total energy converged to within 10^{-5} eV. To better evaluate the van der Waals' interaction, Grimme's method (DFT-D3) was included during the surface adsorption. For integration over the reciprocal space, we used a 3 × 3 × 1 k-point mesh with horizontal shifts. Ab initio molecular dynamics (AIMD) were performed under temperature of 363 K. At each AIMD time step (2 fs for modeling dynamics in all simulations), the total energy is evaluated to an accuracy of 10^{-5} eV per atom employing a plane-wave energy cutoff of 400 eV and a 3 × 3 × 1 k-point mesh. VESTA was used to draw the molecular structure.[6]

Classical MD simulations were performed with the Gromacs 5.1.4 MD software package.[7] L-J parameters with partial charges of Pb^{2+} and I^- were used to simulate phase transition process of $FAPbI_3$.[8] In the simulations, the resulting systems were subject to 100000 steps of steepest descent minimization. The periodic boundary condition was applied in the simulation. The cut-off radius for the Lennard Jones and electrostatic interactions were set to be 10 Å. For accurate evaluation of the long-range Coulomb interactions, Particle Mesh Ewald (PME) summation method is used for electrostatic interactions beyond the cut-off. The system was heated to 363 K in 100 ps by using a v-rescale[9] thermostat for the canonical ensemble (NVT) simulations. During this process, the Linear Constraint Solver (LINCS) algorithm[10] was used to constrain all the bond lengths. The isothermal isobaric ensemble (NPT) was used in the subsequent simulations, with the pressure set to 1 bar in 100 ps, controlled using a v-rescale thermostat and Parrinello-Rahman barostat. Thereafter, the systems were simulated for 100 ns under 363 K. Three repeated MD simulations with different initial velocities were also performed. Throughout the simulations a time step of 2.0 fs was used.

Supplementary Text

Basicity of solvents

The testing mechanisms and objects of donor number (DN) and Kamlet-Taft β values were different. O atom of solvent molecules could attack the $SbCl_5$ to form Sb-O bonds, and DN value was based on the reaction heat from the solvents dissolved in CH_2ClCH_2Cl and $SbCl_5$. Hence, the DN value of solvent can reflect coordination strengthen of solvents with Lewis basic species; the higher DN, the stronger coordination. By contrast, Kamlet-Taft β was defined as the difference in the maximum absorbance of two dyes (4-nitroaniline and *N*,*N*-diethyl-4-nitroaniline), resulting from that one dye had an acidic proton. To a certain degree, the β value can reflect the formation capacity of hydrogen bonds between solvents and Lewis basic species. The higher β, the stronger hydrogen bonds.

Measurement of DN and Kamlet-Taft β values

Measurement of DN: ^{23}Na NMR was used to estimate the DN values of solvents. Here we exploited the linear trend of DN values against ^{23}Na NMR shifts and extracted the DN values of solvents from this trend,[11-14] and ^{23}Na NMR test was carried out in a 0.2-M solution of NaClO$_4$. Using these data, the DN values of PDI and TMSO were estimated to be 24.4 and 28.0 kcal/mol, respectively.

Measurement of Kamlet-Taft β: ^{19}F NMR was used to estimate the β values of solvents.[15-18] NMR measurements were conducted by 4-fluorophenol (less than 0.01 mol/L) and 4-fluoroanisole (less than 0.1 mol/L) solutions. The NMR tube contained an inserted capillary of hexafluorobenzene/CDCl$_3$ solution (v./v. varying from 0.05% to 0.5%) as an external standard, and the chemical shifts were reported relative to $\delta\ [^{19}\mathrm{F}\ (\mathrm{C_6F_6})] = -162.2$ ppm. Hydrogen-bonds induced chemical shifts could be calculated by

$\Delta\{-\delta[(^{19}\mathrm{F})\ (\mathrm{OH - OMe})]\} = -\delta[(^{19}\mathrm{F})\ (\mathrm{OH})] - \{-1.009\delta[(^{19}\mathrm{F})\ (\mathrm{OMe})] - 1.257\}$

The β values were calculated by $\beta = \Delta\{-\delta[(^{19}\mathrm{F})\ (\mathrm{OH - OMe})]\}/3.395$.

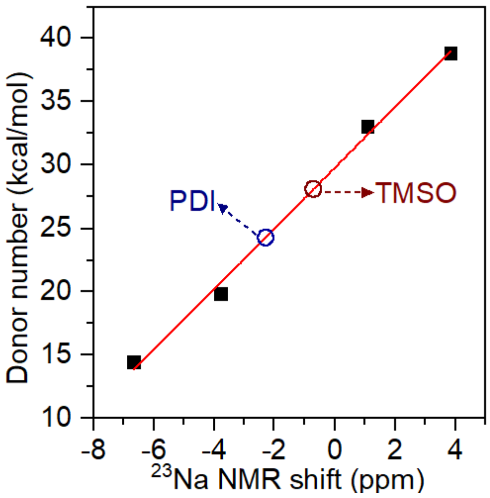

Figure S1. Plot of ^{23}Na NMR shifts versus DN values from corresponding solvents. The fitted line was Y=29.77 + 2.39X. X represented the ^{23}Na NMR shifts and Y represented the DN values. The DN values of used solvents are listed in Table S1.

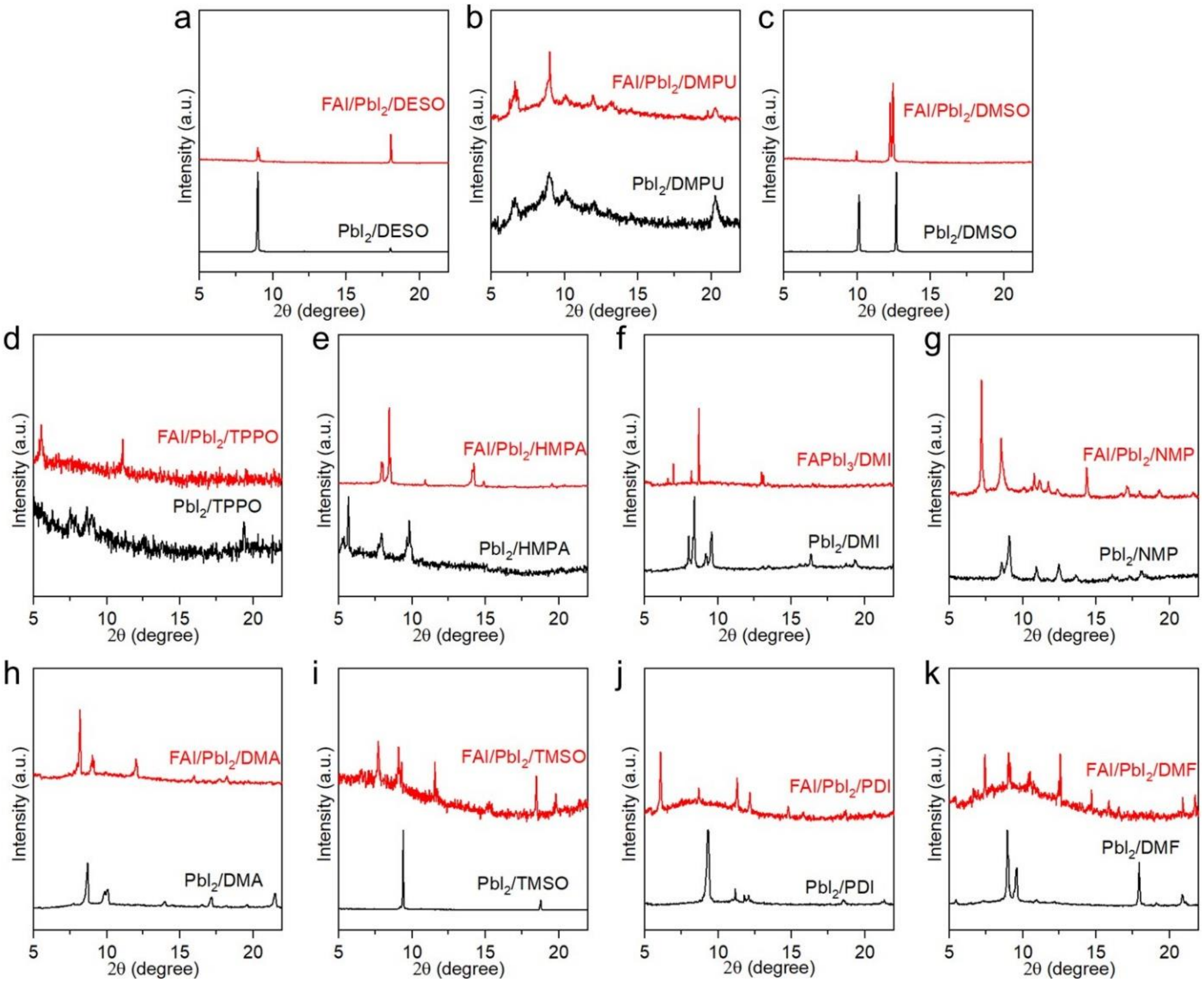

Figure S2. (a-c) XRD patterns of crystals grown from different solutions in the case of $\beta <$ DN*: (a) PbI$_2$/DESO and FAI/PbI$_2$/DESO, (b) PbI$_2$/DMPU and FAI/PbI$_2$/DMPU, (c) PbI$_2$/DMSO and FAI/PbI$_2$/DMSO. The same XRD results from PbI$_2$/OXRs and FAI/PbI$_2$/OXRs demonstrated the Pb-O coordination within PbI$_2$-OXR structures. (d-k) XRD patterns of crystals grown from different solutions in the case of $\beta \geq$ DN*: (d) PbI$_2$/TPPO and FAI/PbI$_2$/TPPO, (e) PbI$_2$/HMPA and FAI/PbI$_2$/HMPA, (f) PbI$_2$/DMI and FAI/PbI$_2$/DMI, (g) PbI$_2$/NMP and FAI/PbI$_2$/NMP, (h) PbI$_2$/DMA and FAI/PbI$_2$/DMA, (i) PbI$_2$/TMSO and FAI/PbI$_2$/TMSO, (j) PbI$_2$/PDI and FAI/PbI$_2$/PDI, (k) PbI$_2$/DMF and FAI/PbI$_2$/DMF. The different results from PbI$_2$/OXRs and FAI/PbI$_2$/OXRs indicated the formation of OXRs-intercalation (FA···OXR)PbI$_3$ structures from FAI/PbI$_2$/OXRs solutions.

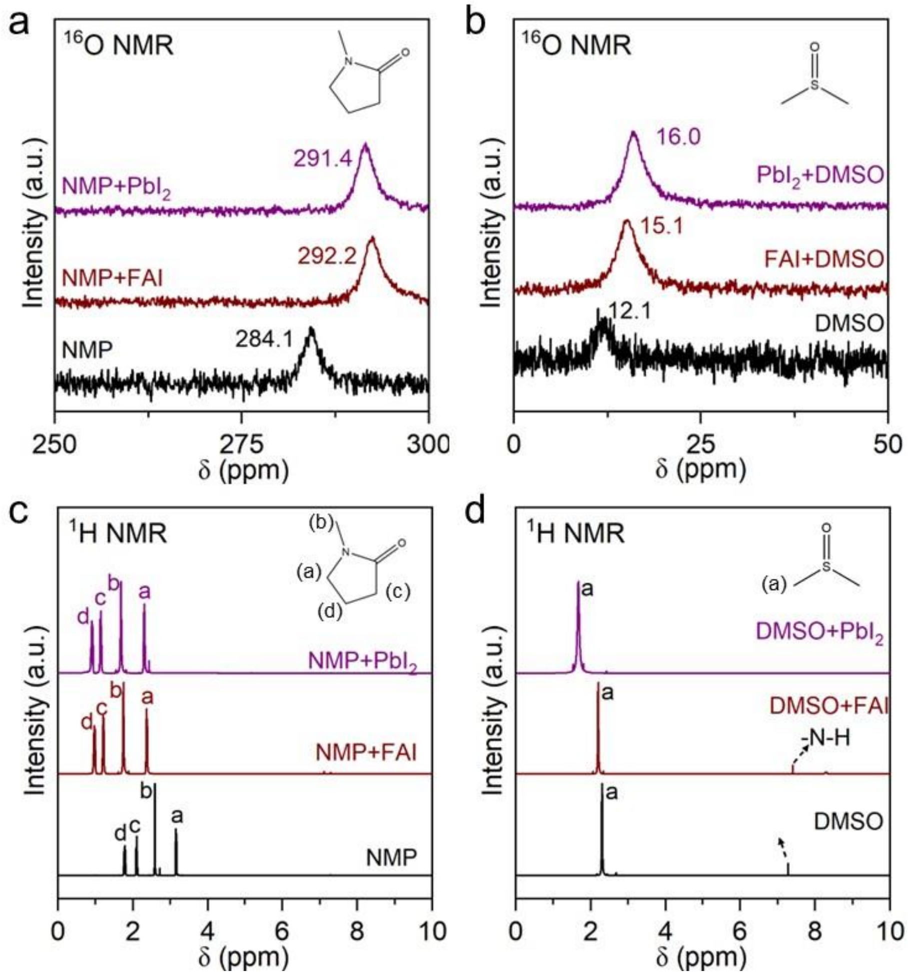

Figure S3. (a,b) ^{16}O and (c,d) ^{1}H NMR spectra of FAI and PbI$_2$ precursors in solvents. CDCl$_3$ was used as an external reference for NMR measurements.

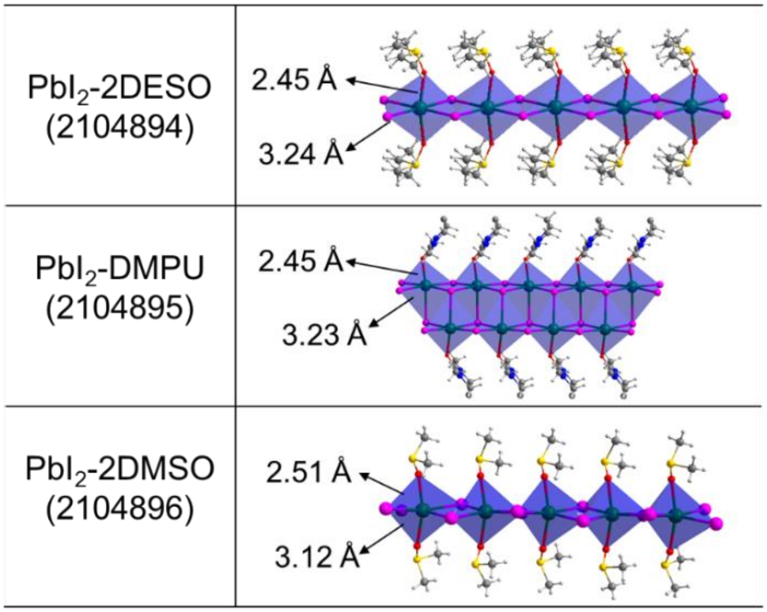

Figure S4. Single crystal structures of PbI_2-OXR crystals (see Table S4). Both PbI_2-2DMSO and PbI_2-2DESO structures exhibit a single-chain type of edge-shared PbI_4O_2 octahedra, and the PbI_2-DMPU structure exhibits a double-chain type of edge-shared PbI_5O octahedra. CCDC numbers were shown in the parenthesis. Color legend: pink, I; green, Pb; red, O; yellow, S; grey, C; blue, N; white, H.

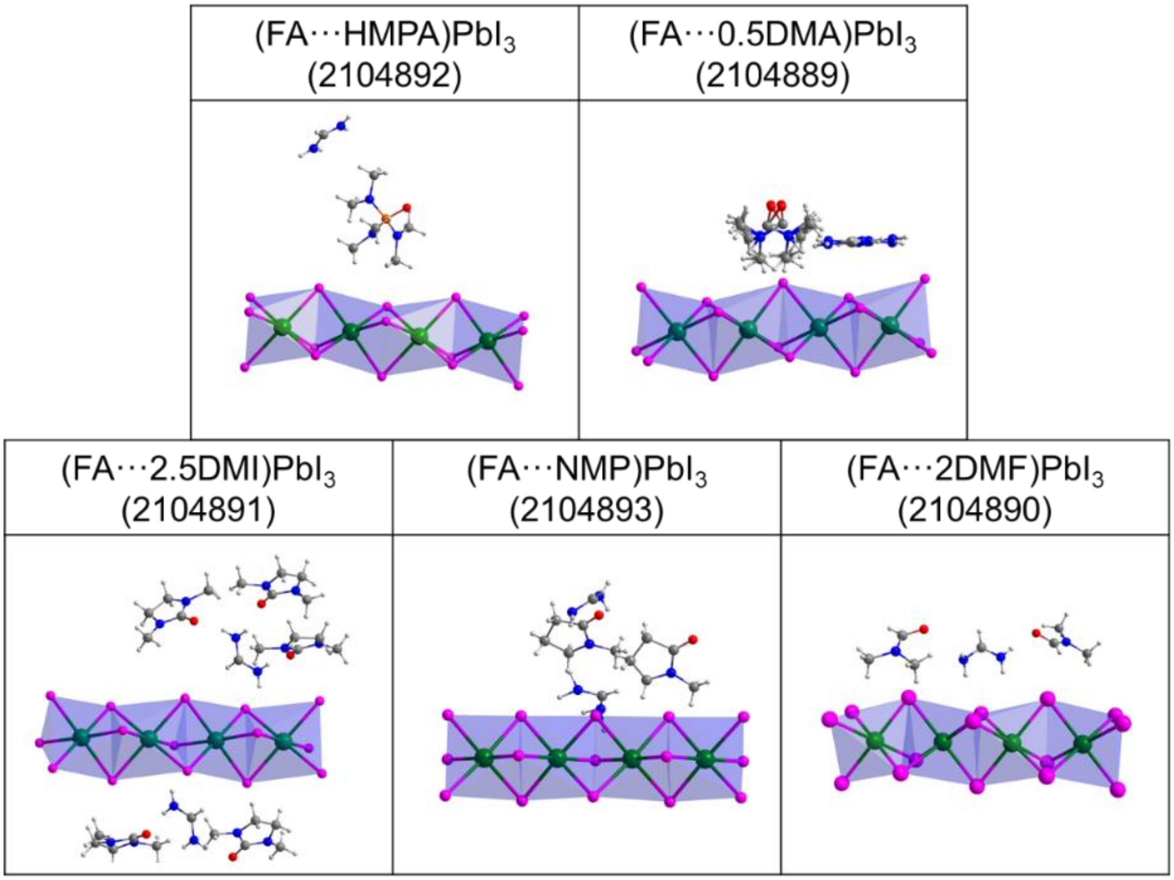

Figure S5. Single crystal structures of (FA···OXR)PbI_3 crystals (see Table S5). All (FA···OXR)PbI_3 structures display a face-shared PbI_6 octahedra with different stoichiometric ratio of OXRs and FA^+ counter ions. CCDC numbers were shown in the parenthesis. Color legend: pink, I; green, Pb; red, O; grey, C; orange, P; blue, N; white, H.

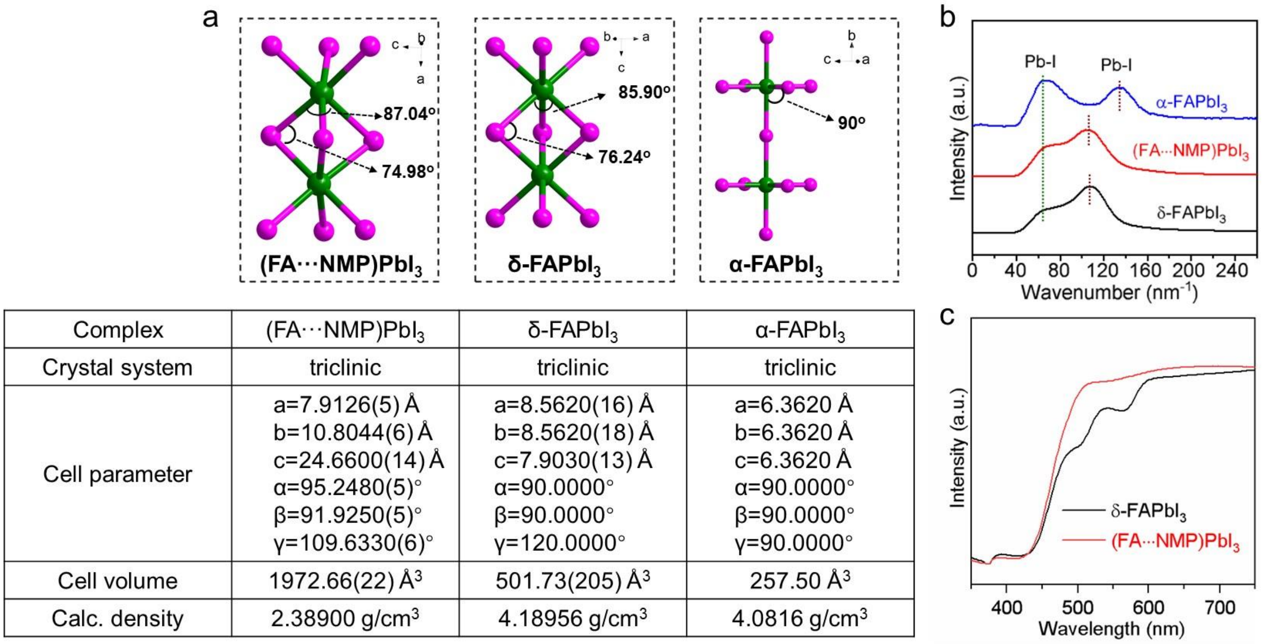

Complex	(FA···NMP)PbI$_3$	δ-FAPbI$_3$	α-FAPbI$_3$
Crystal system	triclinic	triclinic	triclinic
Cell parameter	a=7.9126(5) Å b=10.8044(6) Å c=24.6600(14) Å α=95.2480(5)° β=91.9250(5)° γ=109.6330(6)°	a=8.5620(16) Å b=8.5620(18) Å c=7.9030(13) Å α=90.0000° β=90.0000° γ=120.0000°	a=6.3620 Å b=6.3620 Å c=6.3620 Å α=90.0000° β=90.0000° γ=90.0000°
Cell volume	1972.66(22) Å^3	501.73(205) Å^3	257.50 Å^3
Calc. density	2.38900 g/cm^3	4.18956 g/cm^3	4.0816 g/cm^3

Figure S6. (a) I-Pb-I bond angles of different PbI$_6$ octahedral species and corresponding crystal parameters (FA$^+$ cations and NMP molecules are omitted here). (b) Raman spectra of α-FAPbI$_3$, (FA···NMP)PbI$_3$ and δ-FAPbI$_3$ crystals. The similar Pb-I vibration of δ-FAPbI$_3$ and (FA···NMP)PbI$_3$ demonstrated the similar connection mode of PbI$_6$ octahedra, different from that of α-FAPbI$_3$ with corner-shared PbI$_6$ octahedra. (c) UV-vis absorption spectra of δ-FAPbI$_3$ and (FA···NMP)PbI$_3$ crystals.

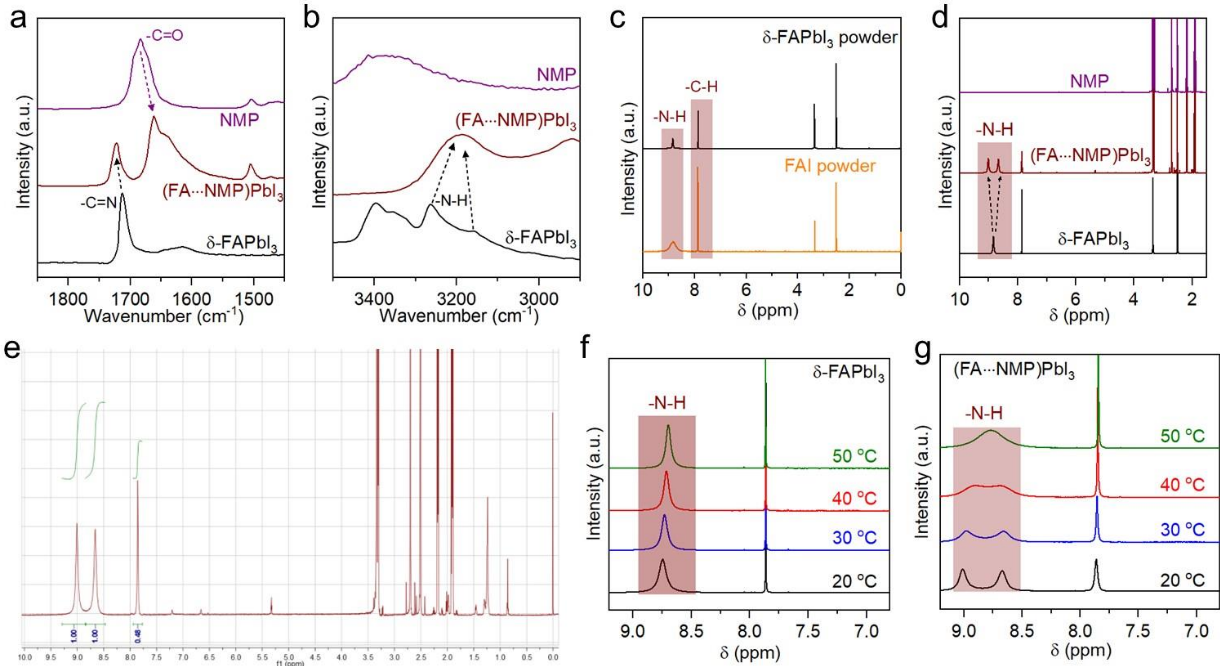

Figure S7. (a,b) ATR-FTIR of (FA···NMP)PbI_3, δ-$FAPbI_3$ and NMP. (c,d) ^{1}H NMR spectra of δ-$FAPbI_3$, FAI, (FA···NMP)PbI_3 and NMP tested at room temperature. (e) ^{1}H NMR spectrum of (FA···NMP)PbI_3 crystals from Figure S7d. The integrated area of two splitting peaks among 8.5~9.5 ppm was equal. *In-situ* ^{1}H NMR spectra of (f) δ-$FAPbI_3$ and (g) (FA···NMP)PbI_3 crystals tested from 20 to 50 °C. DMSO-d6 was chose as deuterated reagent.

ATR-FTIR characterizations (Figure S7a) display an obvious blue shift of -C=N stretching vibration (FA^+ cations) for (FA···NMP)PbI_3, compared to δ-$FAPbI_3$, due to the formation of hydrogen bonds between FA^+ and NMP. Correspondingly, the -C=O peak of NMP in (FA···NMP)PbI_3 shows a red shift, compared to pristine NMP. Not only the C=O (from NMP molecule) and C=N (from FA^+) signals but also the change of -N-H signal from (FA···NMP)PbI_3 were observed (Figure S7b). Room-temperature ^{1}H NMR spectra (Figure S7c) show that the same broad peaks at 8.83 ppm from FAI and δ-$FAPbI_3$ are assigned to -N-H resonance of FA^+ cations. However, upon the formation of (FA···NMP)PbI_3, this single peak is split into two symmetric peaks at 9.00 and 8.66 ppm (Figure S7d,e). Temperature-dependent ^{1}H NMR spectra show that these two split peaks of -N-H in (FA···NMP)PbI_3 experienced a gradually merging process from 20 to 50 °C, but little influence on the -N-H single peak of δ-$FAPbI_3$ (Figure S7f,g). The higher temperature, the weaker hydrogen bonds between FA^+ and NMP. Consequently, above results demonstrate the stable intercalation of NMP into (FA···NMP)PbI_3 lattice by FA···NMP hydrogen bonds.

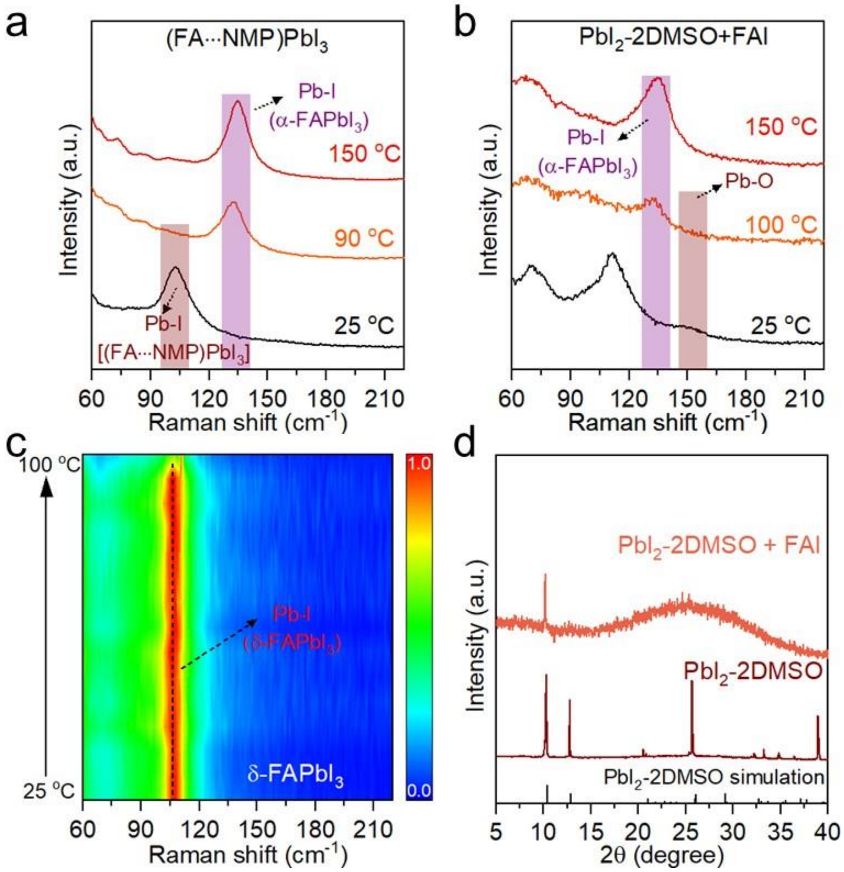

Figure S8. Raman spectra of (a) (FA···NMP)PbI_3 and (b) PbI_2-2DMSO + FAI (grinding mixture) from Figure 2b,c. (c) *In-situ* temperature-dependent Raman spectra of δ-$FAPbI_3$ crystals. (d) XRD patterns of PbI_2-2DMSO and PbI_2-2DMSO + FAI (grinding mixture) crystals.

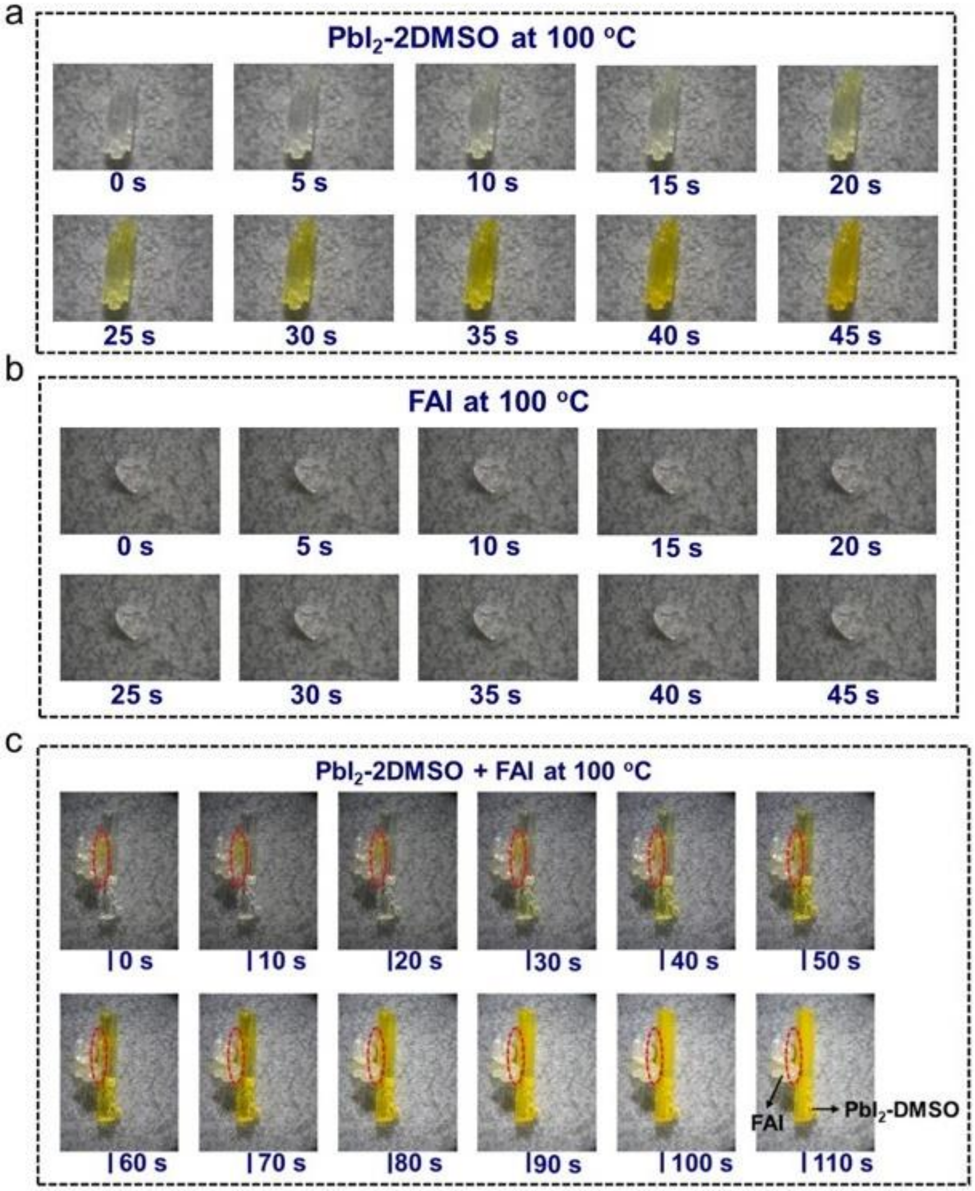

Figure S9. Photographs of (a) PbI_2-2DMSO, (b) FAI, and (c) PbI_2-2DMSO + FAI (grinding mixture) crystals subjected to heating at 100 ^{o}C.

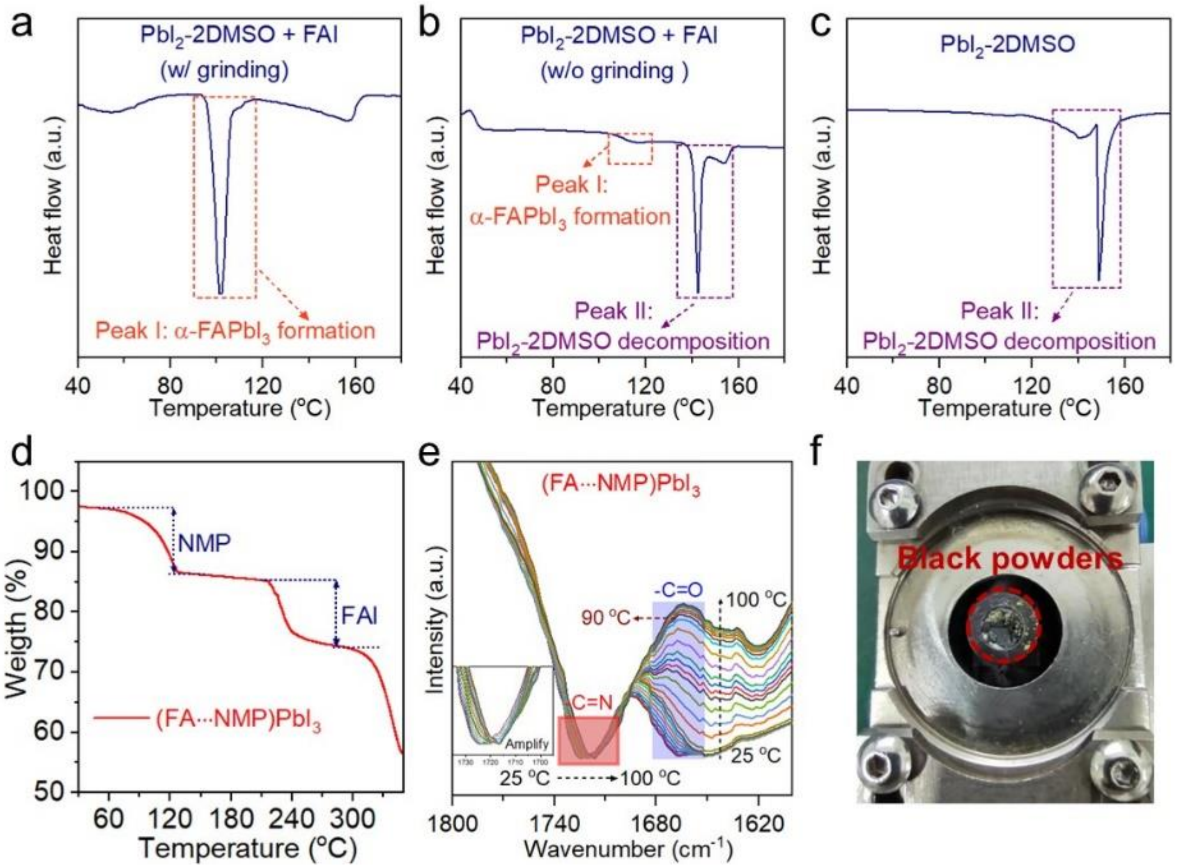

Figure S10. DSC curves of (a) PbI_2-2DMSO + FAI (grinding), (b) PbI_2-2DMSO + FAI (without grinding) and (c) PbI_2-2DMSO powders. Peak I: the low-temperature peak. Peak II: the high-temperature peak. (d) Thermogravimetric analysis and (e) *in-situ* ATR-FTIR characterization of (FA···NMP)PbI_3 crystals during heating under N_2. (f) *In-situ* pool of ATR-FTIR measurement. The gradual shifts of -C=N signal and the disappearance of -C=O signal with increasing temperatures recorded the NMP removing process from (FA···NMP)PbI_3 lattice, and the formation of black powders within *in-situ* pool indicated the α-$FAPbI_3$ formation.

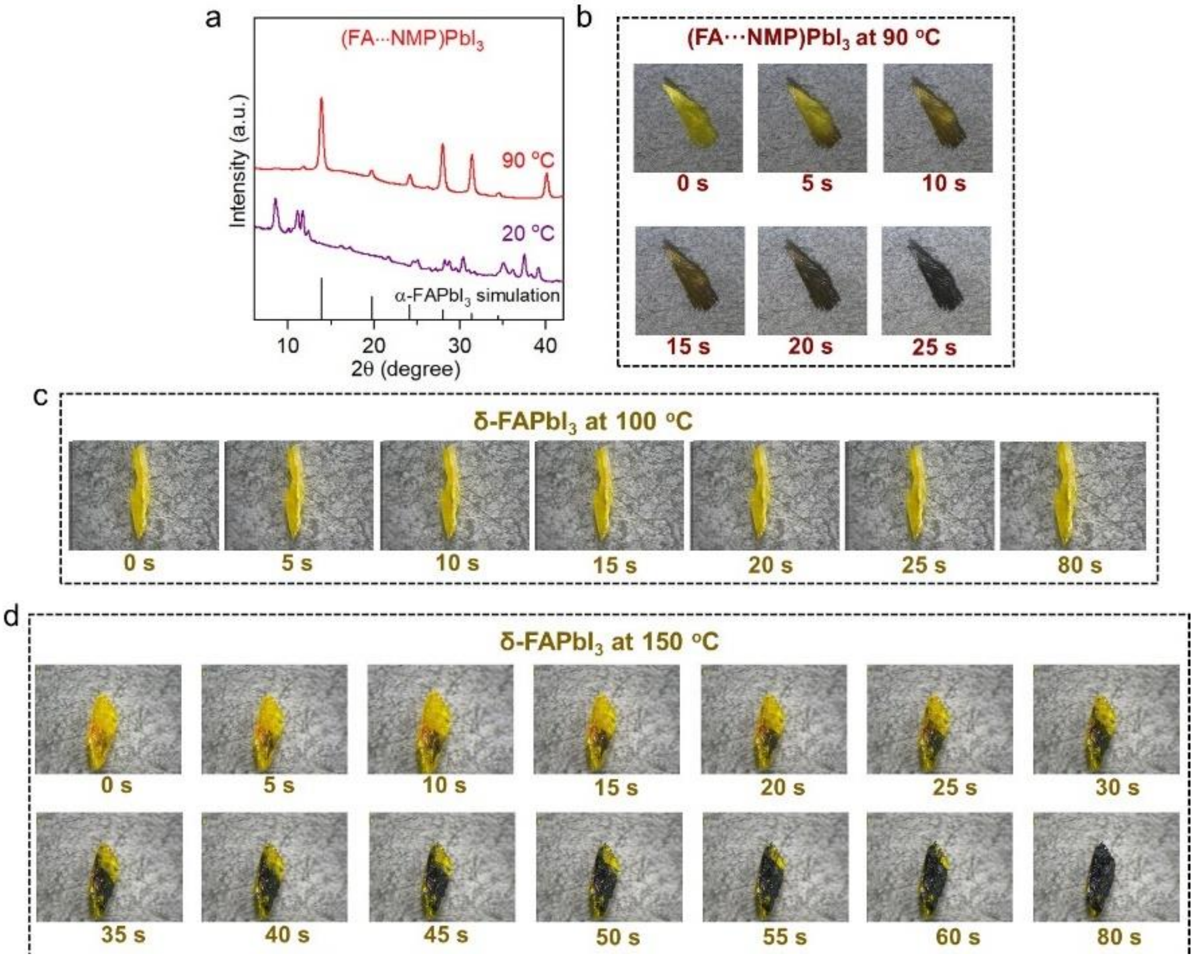

Figure S11. (a) *In-situ* single crystal XRD patterns of a single (FA···NMP)PbI$_3$ crystal. (b) Photographs of (FA···NMP)PbI$_3$ crystals subjected to heating at 90 °C. Photographs of δ-FAPbI$_3$ crystals subjected to heating at (c) 100 °C and (d) 150 °C.

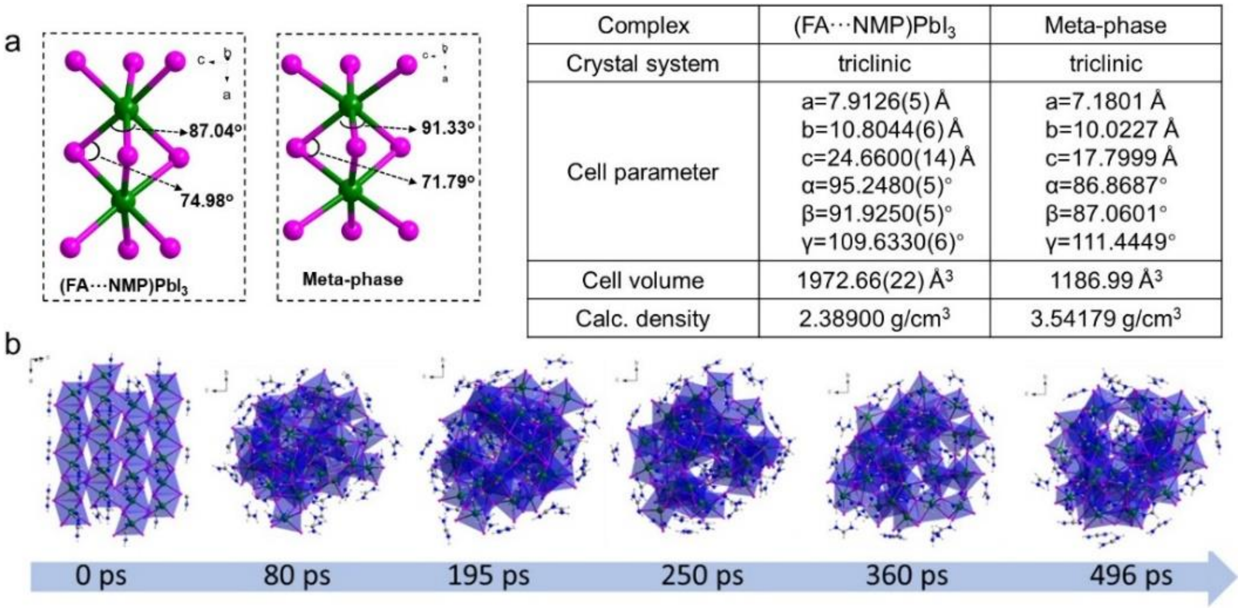

Complex	(FA···NMP)PbI$_3$	Meta-phase
Crystal system	triclinic	triclinic
Cell parameter	a=7.9126(5) Å b=10.8044(6) Å c=24.6600(14) Å α=95.2480(5)° β=91.9250(5)° γ=109.6330(6)°	a=7.1801 Å b=10.0227 Å c=17.7999 Å α=86.8687° β=87.0601° γ=111.4449°
Cell volume	1972.66(22) Å^3	1186.99 Å^3
Calc. density	2.38900 g/cm^3	3.54179 g/cm^3

Figure S12. (a) I-Pb-I bond angles of metastable phase and corresponding crystal parameters (FA$^+$ cations and NMP molecules are omitted here), demonstrating the deformation of PbI$_6$ octahedral framework of metastable phase. (b) AIMD simulated transforming path of metastable phase at 363 K. At the beginning, the adjacent isolated octahedral polytypes connected with neighboring octahedra by I-vertexes. The crowded polytypes moved and produced more corner-shared PbI$_6$ octahedra during time scale, exhibiting the favourable conversion trend towards α-FAPbI$_3$ at 363 K.

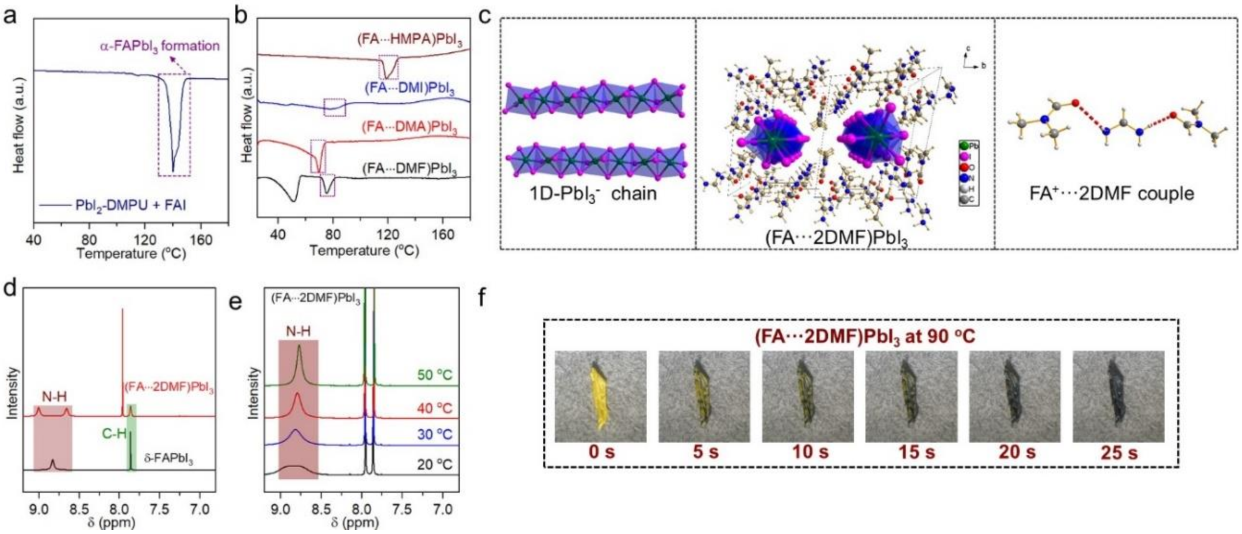

Figure S13. DSC curves of (a) PbI_2-OXR + FAI (grinding mixture) and (b) (FA···OXR)PbI_3 powders. (c) Single crystal analysis of the (FA···2DMF)PbI_3 structure. (d) ^{1}H NMR and (e) *in-situ* ^{1}H NMR spectra of (FA···2DMF)PbI_3 crystals. The peak of -N-H from (FA···2DMF)PbI_3 had a splitting phenomenon at room temperature but underwent gradual merging with increasing temperatures, due to the hydrogen bonds between FA^+ and DMF molecules. (f) Photographs of (FA···2DMF)PbI_3 crystals subjected to heating at 90 ^{o}C.

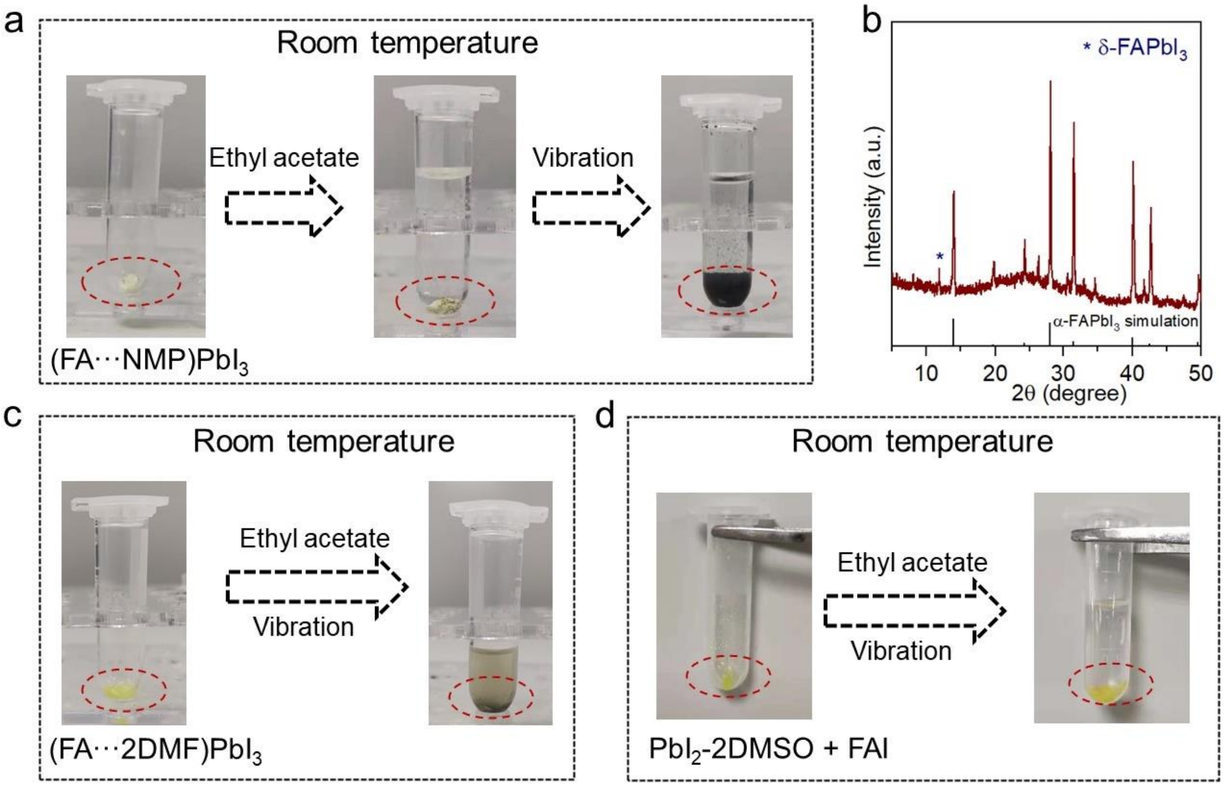

Figure S14. (a) Photographs of (FA···NMP)PbI_3 crystals before and after ethyl acetate treatment. (b) XRD pattern of black powders from Figure S14a. The pale-yellow crystals turned black after introducing ethyl acetate, indicating the α-$FAPbI_3$ formation at room temperature. The coexistence of δ-$FAPbI_3$ and α-$FAPbI_3$ might be due to incomplete transformation or the self-instability characteristics of α-$FAPbI_3$ after exposing to the atmosphere during XRD measurement. Photographs of (c) (FA···2DMF)PbI_3 and (d) PbI_2-2DMSO + FAI powders (grinding mixture) before and after ethyl acetate treatment.

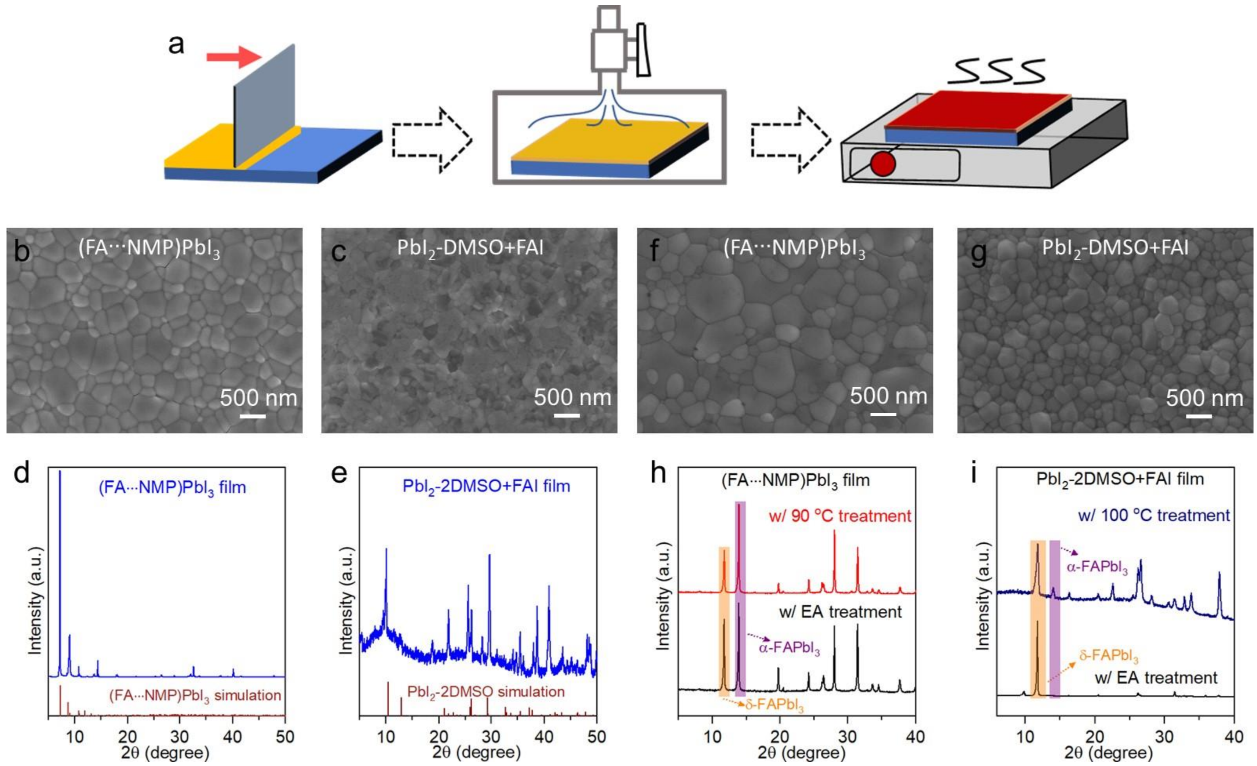

Figure S15. (a) Scheme showing the vacuum-flash assisted blade-coating technology. The residual solvents within wet film are extracted to form intermediate film in the vacuum-flash step. (b, c) SEM images and (d, e) XRD patterns of intermediate films made from (FA···NMP)PbI$_3$ and PbI$_2$-2DMSO (with FAI addition) powders in 2ME solution. SEM images of (f) (FA···NMP)PbI$_3$ intermediate film by annealing at 90 ^{o}C and (g) PbI$_2$-2DMSO (with FAI addition) intermediate film by annealing at 100 ^{o}C. XRD patterns of FAPbI$_3$ films obtained from (h) (FA···NMP)PbI$_3$ intermediate film by annealing at 90 ^{o}C or treating with ethyl acetate, and (i) PbI$_2$-2DMSO (with FAI addition) intermediate film by annealing at 100 ^{o}C or treating with ethyl acetate at room temperature.

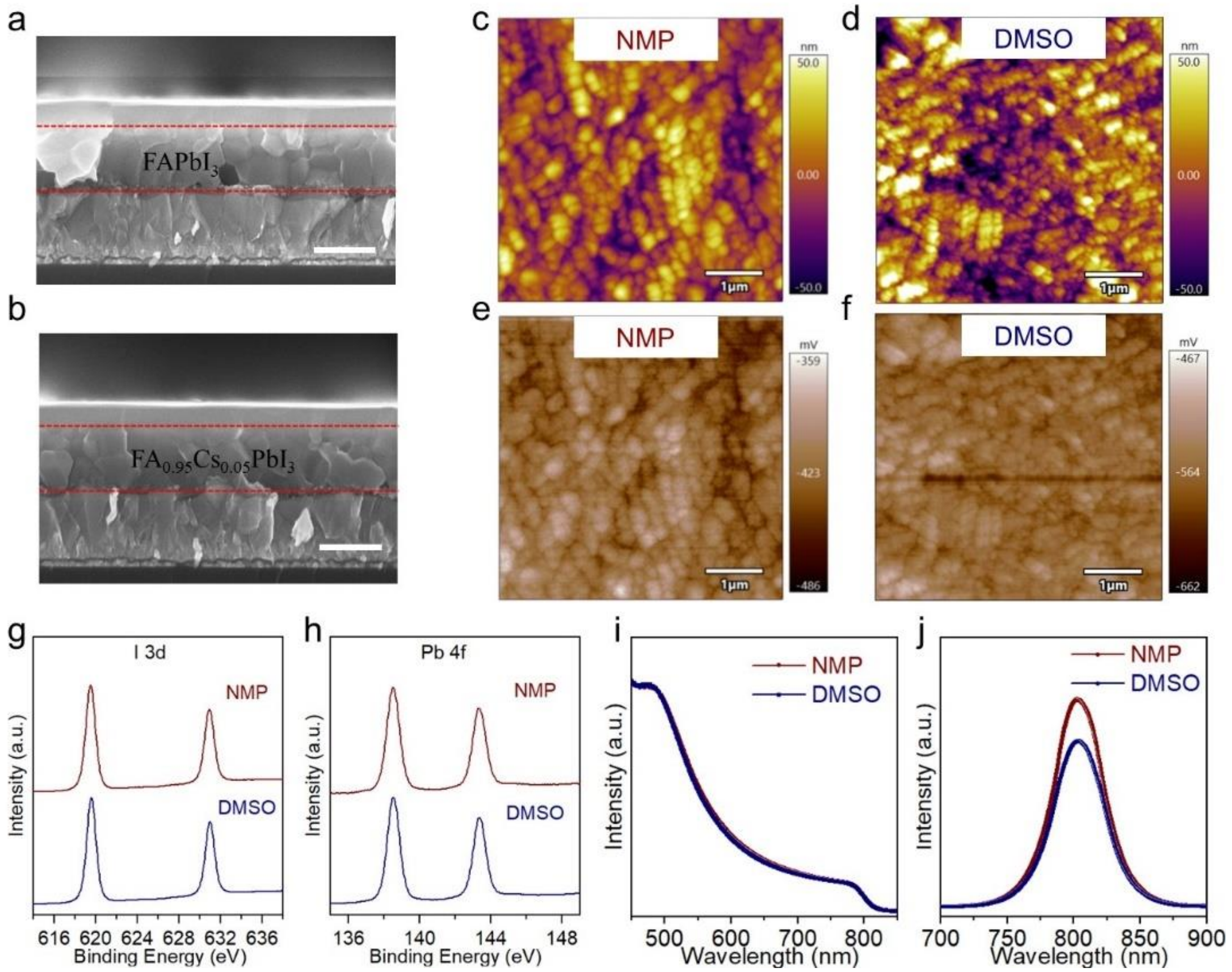

Figure S16. Cross-sectional SEM images of (a) pure FAPbI$_3$ film and (b) FAPbI$_3$-based film (with Cs$^+$ and PbCl$_2$ additives) obtained from (FA···NMP)PbI$_3$ intermediates by 90 ^{o}C annealing. The scale bar is 500 nm. Atomic force microscope (AFM) and kelvin probe force microscope (KPFM) images of (c,e) NMP-film and (d,f) DMSO-film. The NMP-film had a lower roughness of 15.80 nm compared with the DMSO-film (22.42 nm). High-resolution XPS spectra of (g) Pb and (h) I in the surface of the NMP-film and DMSO-film. XPS by integrating the spectra with respect to the Pb 4f and I 3d peaks was used to investigate the difference of I/Pb composition. (i) UV-vis and (j) PL spectra of the NMP-film and DMSO-film.

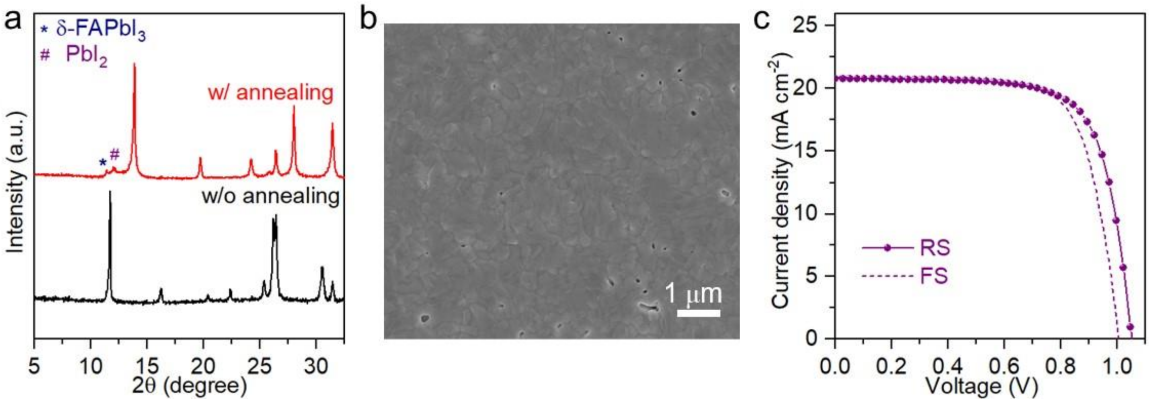

Figure S17. (a) XRD patterns of as-prepared $FAPbI_3$ films transferred from δ-$FAPbI_3$ before and after annealing at 150 °C. (b) Top-view SEM image of as-annealed α-$FAPbI_3$ film and (c) *J*-*V* curves of the resembled device from corresponding film. The precursor was prepared by dissolving the FAI and PbI_2 powders in 2ME without OXRs, as same as abovementioned precursor preparation. The α-$FAPbI_3$ film by annealing at 150 °C accompanied with undesirable δ-$FAPbI_3$ and PbI_2, and the resembled device exhibited PCE of 15.81% in reverse scan and 15.16% in forward scan.

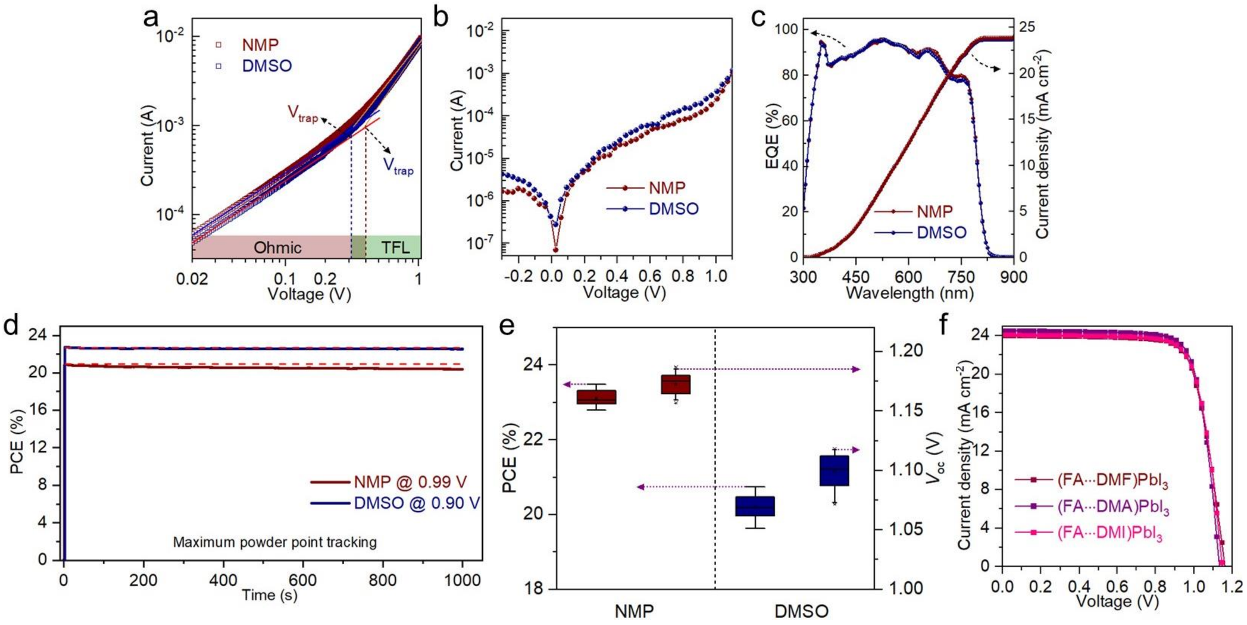

Figure S18. (a) Space charge limited current (SCLC) measurements for the devices (FTO/ZnTiO$_3$/Perovskite/PCBM/Au). (b) Dark current densities, (c) IPCE measurements, and (d) operational stability of the NMP-PSC and DMSO-PSC. (e) Statistics of PCE and V_{OC} analyzed on 20 individual PSCs. (f) *J-V* curves of (FA···OXR)PbI$_3$ based devices. The precursors with additives were prepared as same as abovementioned precursor preparation, and the mole ratio of OXRs relative to FAPbI$_3$ was 2:1, 0.5:1 and 2.5:1 for DMF, DMA and DMI-based precursors, respectively. The as-prepared films after vacuum flashing were annealed at 100 ^{o}C. The PSCs from the DMF-film, DMA-film and DMI-film displayed PCEs of 21.08%, 21.57% and 20.98%, respectively.

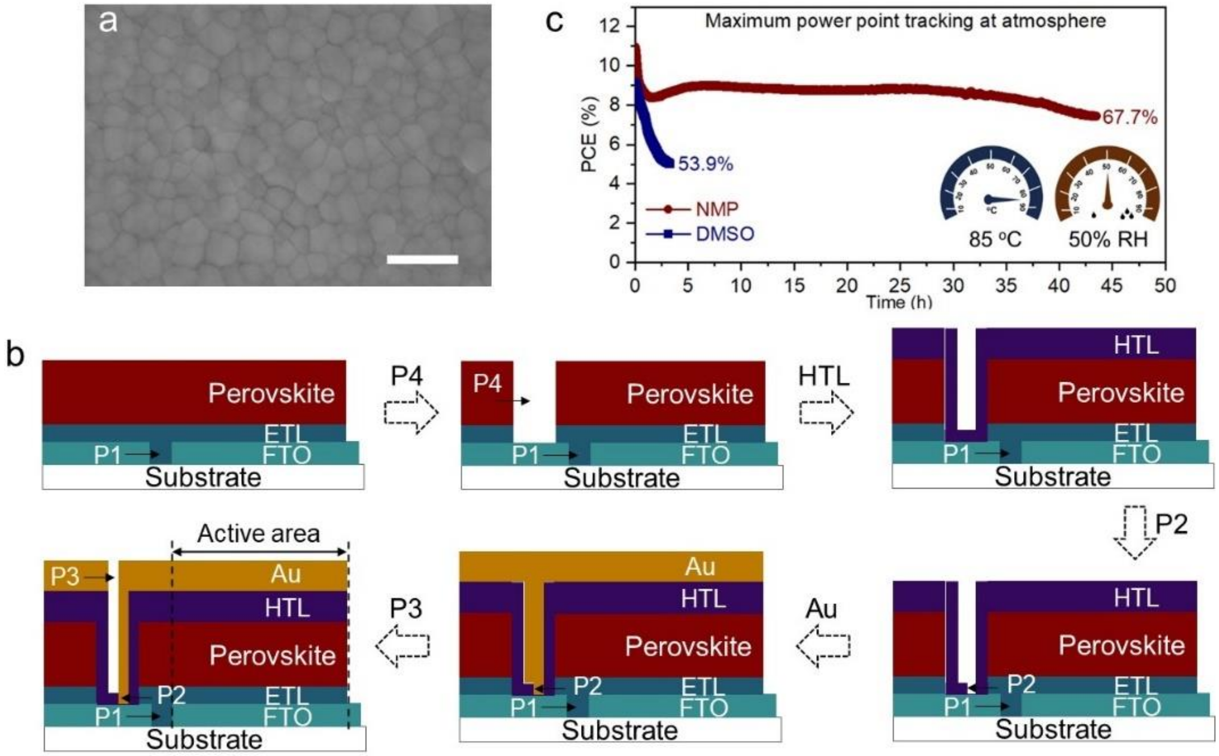

Figure S19. (a) SEM images of 6 × 6 cm^2 NMP-film. The scale bar is 500 nm. (b) Diagrammatic sketch of a module, including P1, P2, P3 and P4. (c) Maximum power point tracking of encapsulated modules under harsh hydrothermal condition (85 °C and 50% RH%). While both modules lost lot of PCE at the beginning, the NMP-module recovered partial current and maintained stable over 40 hours. By contrast, the DMSO-module dropped 53.9 % of initial PCE after 3 hours.

Table S1. DN values of solvents and corresponding ^{23}Na NMR shifts of $NaClO_4$ dissolved in them.

Solvent	^{23}Na NMR shift (ppm)	DN (kcal/mol)	DN* (DN/38.8)
ACN	-6.65	14.4	0.37
2ME	-3.78	19.8	0.51
PDI	-2.25	24.4	0.63
TMSO	-0.75	28.0	0.72
DMPU	1.30	33.0	0.85
HMPA	3.85	38.8	1.00

Table S2. Kamlet-Taft β values calculated by ^{19}F NMR shifts.

Solvent	-δ(^{19}F)(OH)	-δ(^{19}F)(OMe)	Δ_1[-δ(^{19}F)(OH-OMe)]	β
2ME	127.56	125.79	1.89	0.62
DMF	127.73	125.77	2.10	0.69
DMI	127.76	125.67	2.21	0.73
DESO	126.70	124.50	2.35	0.77
TPPO	129.10	125.94	3.30	1.09

Table S3. Basicity parameters of solvents.

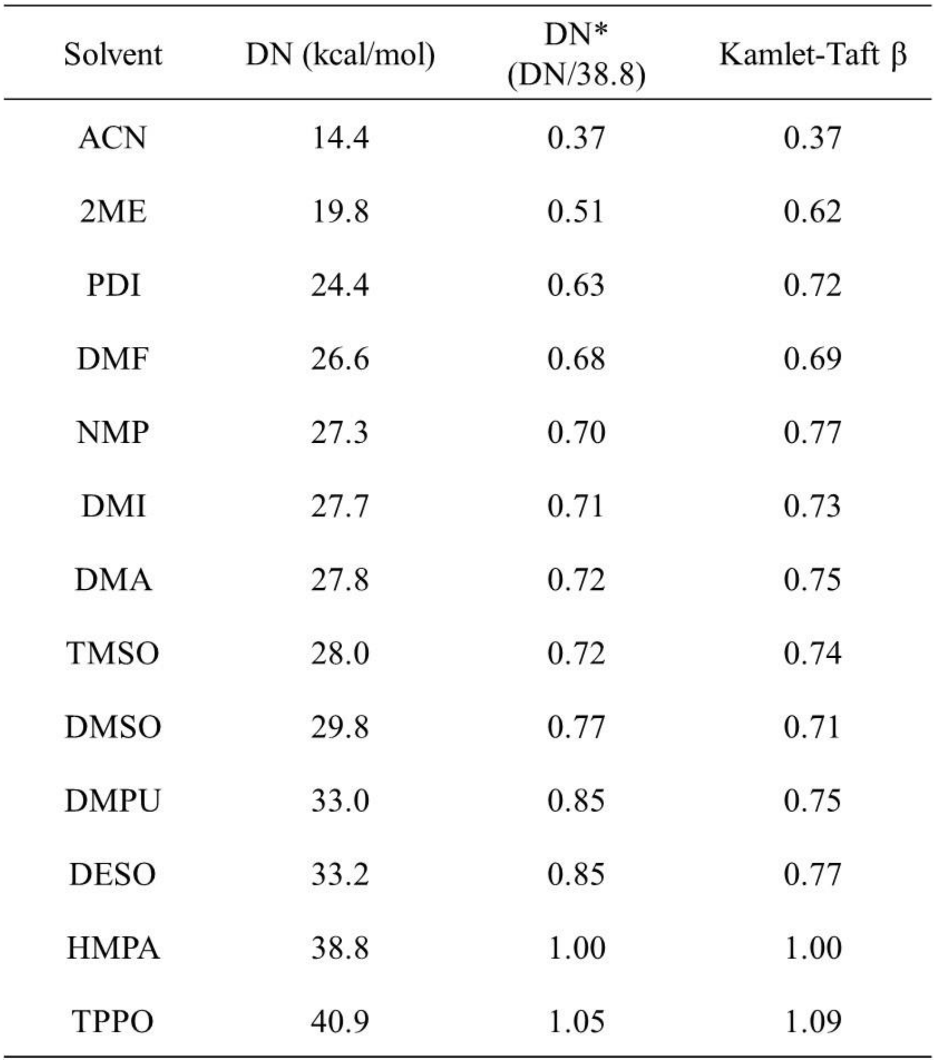

Solvent	DN (kcal/mol)	DN* (DN/38.8)	Kamlet-Taft β
ACN	14.4	0.37	0.37
2ME	19.8	0.51	0.62
PDI	24.4	0.63	0.72
DMF	26.6	0.68	0.69
NMP	27.3	0.70	0.77
DMI	27.7	0.71	0.73
DMA	27.8	0.72	0.75
TMSO	28.0	0.72	0.74
DMSO	29.8	0.77	0.71
DMPU	33.0	0.85	0.75
DESO	33.2	0.85	0.77
HMPA	38.8	1.00	1.00
TPPO	40.9	1.05	1.09

Table S4. Crystal data and structure refinement of PbI_2-OXR.

Complex	PbI_2-2DESO	PbI_2-DMPU	PbI_2-2DMSO
Empirical formula	$C_8H_{20}I_2O_2PbS_2$	$C_6H_{12}I_2N_2OPb$	$C_4H_{12}I_2O_2PbS_2$
Formula weight	673.35	589.17	617.25
Temperature/K	100.01(10)	193.0	100.00(10)
Crystal system	orthorhombic	monoclinic	orthorhombic
Space group	*Fdd*2	$P2_1/n$	*Pccn*
a/Å	28.8096(17)	15.5062(15)	13.6992(4)
b/Å	26.4452(15)	4.5372(4)	10.8620(4)
c/Å	4.5530(3)	18.2167(18)	8.7610(2)
α/°	90	90	90
β/°	90	107.874(5)	90
γ/°	90	90	90
Volume/Å^3	3468.8(4)	1219.8(2)	1303.64(7)
Z	8	4	4
ρ_{calcg}/cm^3	2.579	3.208	3.145
μ/mm^{-1}	49.003	45.210	17.963
F(000)	2432.0	1032.0	1088.0
Crystal size/mm^3	0.01×0.01×0.01	0.12×0.1×0.1	0.02×0.01×0.01
Radiation	Cu Kα (λ = 1.54184)	Ga Kα (λ= 1.34139)	Mo Kα (λ = 0.71073)
2Θ range for data collection/°	9.078 to 148.11	8.874 to 121.298	7.504 to 61.002
Index ranges	$-33 \le h \le 35$, $-30 \le k \le 32$, $-5 \le l \le 5$	$-19 \le h \le 19$, $0 \le k \le 5$, $0 \le l \le 23$	$-17 \le h \le 18$, $-10 \le k \le 15$, $-7 \le l \le 12$
Reflections collected	5417	2790	4898
Independent reflections	1610 [R_{int} = 0.0833, R_{sigma} = 0.0541]	2790 [R_{sigma} = 0.0484]	1766 [R_{int} = 0.0373, R_{sigma} = 0.0478]
Data/restraints/parameters	1610/26/81	2790/36/112	1766/0/53
Goodness-of-fit on F^2	1.150	1.143	1.017
Final R indexes [I>=2σ (I)]	R_1 = 0.0552, wR_2 = 0.1491	R_1 = 0.0610, wR_2 = 0.1801	R_1 = 0.0318, wR_2 = 0.0622
Final R indexes [all data]	R_1 = 0.0605, wR_2 = 0.1657	R_1 = 0.0743, wR_2 = 0.1921	R_1 = 0.0448, wR_2 = 0.0702
Largest diff. peak/hole / e Å^{-3}	3.16/-3.07	3.23/-2.39	1.28/-3.55

Table S5. Crystal data and structure refinement of (FA···OXR)PbI$_3$.

Complex	(FA···HMPA)PbI$_3$	(FA···0.5DMA)PbI$_3$	(FA···2.5DMI)PbI$_3$	(FA···NMP)PbI$_3$	(FA···2DMF)PbI$_3$
Empirical formula	$C_7H_{23}I_3N_5OPPb$	$C_6H_{19}I_6N_5OPb_2$	$C_{27}H_{60}I_6N_{14}O_5Pb_2$	$C_{12}H_{28}I_6N_6O_2Pb_2$	$C_7H_{19}I_3N_4O_2Pb$
Formula weight	812.16	1353.04	1836.67	1464.18	779.15
Temperature/K	193(2)	193.0	99.98(10)	100.00(10)	100.01(10)
Crystal system	monoclinic	orthorhombic	triclinic	triclinic	monoclinic
Space group	*P*2$_1$/*c*	*Cmcm*	*P*-1	*P*-1	*C*2/*c*
a/Å	27.765(2) Å	7.9664(5)	7.9996(4)	7.9126(5)	19.6503(10)
b/Å	28.963(2) Å	22.5622(13)	13.7838(7)	10.8044(6)	7.8643(3)
c/Å	8.0928(6)	20.0737(11)	24.1633(6)	24.6600(14)	24.6496(13)
α/°	90°	90	89.953(3)	95.248(5)	90
β/°	98.216(4)	90	83.608(3)	91.925(5)	99.613(5)
γ/°	90°	90	82.455(4)	109.633(6)	90
Volume/Å^3	6441.2(9)	3608.0(4)	2624.6(2)	1972.6(2)	3755.8(3)
Z	8	4	2	2	8
ρ_{calcg}/cm^3	1.675	2.491	2324	2.465	2.756
μ/mm^{-1}	22.676	39.779	9.980	53.385	13.915
F(000)	2912	2320.0	1684.0	1280.0	2768.0
Crystal size/mm^3	0.02×0.01×0.01	0.12×0.1×0.1	0.02×0.01×0.01	0.05×0.01×0.01	0.02×0.01×0.01
Radiation	Mo Kα (λ= 0.71073)	Ga Kα (λ= 1.34139)	Mo Kα (λ= 0.71073)	Cu Kα (λ= 1.54184)	Mo Kα (λ= 0.71073)
2Θ range for data collection/°	1.399 to 54.222	6.816 to 126.836	6.788 to 66.06	7.216 to 133.19	7.282 to 60.744
Index ranges	$-33 \le h \le 23$, $-34 \le k \le 35$, $-9 \le l \le 9$	$-10 \le h \le 10$, $-30 \le k \le 24$, $-18 \le l \le 26$	$-12 \le h \le 10$, $-20 \le k \le 21$, $-35 \le l \le 36$	$-9 \le h \le 9$, $-12 \le k \le 11$, $-29 \le l \le 29$	$-26 \le h \le 15$, $-10 \le k \le 10$, $-32 \le l \le 33$
Reflections collected	44997	13698	31977	12731	9652
Independent reflections	11804 [R_{int} = 0.0812]	2424[R_{int} =0.0666, R_{sigma} = 0.0499]	17507 [R_{int} = 0.0669, R_{sigma} = 0.1678]	6952 [R_{int} = 0.0996, R_{sigma} = 0.1289]	4891 [R_{int} = 0.0446, R_{sigma} = 0.0668]
Data/restraints /parameters	11804/313/327	2424/82/108	17507/495/497	6952/155/231	4891/75/160
Goodness-of-fit on F^2	1.039	1.089	0.997	1.048	1.046
Final R indexes [I>=2σ (I)]	R_1 = 0.1291, wR_2 = 0.3072	R_1 =0.0702, wR_2 = 0.1992	R_1 = 0.0630, wR_2= 0.1008	R_1 = 0.1056, wR_2 = 0.2669	R_1 = 0.0535, wR_2 = 0.1292
Final R indexes [all data]	R_1 = 0.2140, wR_2 = 0.3474	R_1 =0.0719, wR_2 = 0.2015	R_1 = 0.1771, wR_2= 0.1436	R_1 = 0.1293, wR_2 = 0.2845	R_1 = 0.0782, wR_2 = 0.1497
Largest diff. peak/hole / e Å^{-3}	4.019/-3.191	3.58/-2.91	2.49/-1.85	6.03/-4.97	6.88/-2.53

Table S6. Energies of monomer structure of (FA···NMP)PbI_3, metastable phase (removing all the NMP molecules from (FA···NMP)PbI_3), NMP, PbI_2-2DMSO, FAI, DMSO and α-$FAPbI_3$.

Structure	Energy (eV)
(FA···NMP)PbI_3	-151.495990
Metastable phase	-56.425487
NMP	-94.340007
PbI_2-2DMSO	-111.660952
FAI	-47.629667
DMSO	-101.803510
α-$FAPbI_3$	-56.607627

Table S7. Detailed parameters of small-scale devices.

0.12-cm^2	Voltage (V)	J (mA cm^{-2})	FF (%)	PCE (%)
RS:NMP	1.18	24.68	80.46	23.43
FS:NMP	1.17	24.59	78.09	22.47
RS:DMSO	1.08	24.28	78.46	20.57
FS:DMSO	1.05	24.29	76.09	19.41

Table S8. Detail paraments of large-scale devices.

18-cm^2	Voltage (V)	J (mA cm^{-2})	FF (%)	PCE (%)
RS:NMP	8.42	3.00	73.45	18.55
FS:NMP	8.40	2.96	73.33	18.23
RS:DMSO	8.03	3.00	70.31	16.94
FS:DMSO	7.86	3.01	65.52	15.50

References

(1) Han, F.; Wu, Y.; He, R.; Hui, Y.; Yin, J.; Zheng, L.; Wu, B.; Zheng, N. Hyperstable perovskite solar cells without ion migration and metal diffusion based on ZnS segregated cubic $ZnTiO_3$ electron transport layers. *Solar RRL* **2021,** *5*, 2000654.

(2) Kresse, G.; Furthmüller, J. Efficiency of ab-initio total energy calculations for metals and semiconductors using a plane-wave basis set. *Comp. Mater. Sci.* **1996,** *6*, 15-50.

(3) Kresse, G.; Furthmuller, J. Efficient iterative schemes for ab initio total-energy calculations using a plane-wave basis set. *Phys. Rev. B Condens. Matter* **1996,** *54*, 11169-11186.

(4) Blochl, P. E. Projector augmented-wave method. *Phys. Rev. B Condens. Matter* **1994,** *50*, 17953-17979.

(5) Perdew, J. P.; Burke, K.; Ernzerhof, M. Generalized gradient approximation made simple. *Phys. Rev. Lett.* **1996,** *77*, 3865-3868.

(6) Momma, K.; Izumi, F. VESTA 3for three-dimensional visualization of crystal, volumetric and morphology data. *J. Appl. Crystallogr.* **2011,** *44*, 1272-1276.

(7) Abraham, M. J.; Murtola, T.; Schulz, R.; Páll, S.; Smith, J. C.; Hess, B.; Lindahl, E. GROMACS: High performance molecular simulations through multi-level parallelism from laptops to supercomputers. *SoftwareX* **2015,** *1-2*, 19-25.

(8) Gutierrez-Sevillano, J. J.; Ahmad, S.; Calero, S.; Anta, J. A. Molecular dynamics simulations of organohalide perovskite precursors: solvent effects in the formation of perovskite solar cells. *Phys. Chem. Chem. Phys.* **2015,** *17*, 22770-7.

(9) Bussi, G.; Donadio, D.; Parrinello, M. Canonical sampling through velocity rescaling. *J. Chem. Phys.* **2007,** *126*, 014101.

(10) Hess, B.; Bekker, H.; Berendsen, H. J. C.; Fraaije, J. G. E. M. LINCS: A linear constraint solver for molecular simulations. *J. Comput. Chem.* **1997,** *18*, 1463-1472.

(11) Marcus, Y. The effectivity of solvents as electron pair donors. *J. Solution Chem.* **1984,** *13*, 599-624.

(12) Erlich, R. H.; Popov, A. I. Spectroscopic studies of ionic solvation. X. Study of the solvation of sodium ions in nonaqueous solvents by sodium-23 nuclear magnetic resonance. *J. Am. Chem. Soc.* **2002,** *93*, 5620-5623.

(13) Johnson, L.; Li, C.; Liu, Z.; Chen, Y.; Freunberger, S. A.; Ashok, P. C.; Praveen, B. B.; Dholakia, K.; Tarascon, J. M.; Bruce, P. G. The role of LiO_2 solubility in O_2 reduction in aprotic solvents and its consequences for Li-O_2 batteries. *Nat. Chem.* **2014,** *6*, 1091-1099.

(14) Cataldo, F. A revision of the Gutmann donor numbers of a series of phosphoramides including TEPA. *Eur. Chem. Bull.* **2015,** *4*, 92-97.

(15) Laurence, C.; Legros, J.; Nicolet, P.; Vuluga, D.; Chantzis, A.; Jacquemin, D. Solvatomagnetic comparison method: a proper quantification of solvent hydrogen-bond basicity. *J. Phys. Chem. B* **2014,** *118*, 7594-7608.

(16) Laurence, C.; Legros, J.; Chantzis, A.; Planchat, A.; Jacquemin, D. A database of dispersion-induction DI, electrostatic ES, and hydrogen bonding alpha1 and beta1 solvent parameters and some applications to the multiparameter correlation analysis of solvent effects. *J. Phys. Chem. B* **2015,** *119*, 3174-3184.

(17) Laurence, C.; Mansour, S.; Vuluga, D.; Legros, J. Measurement of the hydrogen bond acceptance of ionic liquids and green solvents by the 19F solvatomagnetic comparison method. *Green Chem.* **2021,** *23*, 1816-1822.

(18) Laurence, C.; Mansour, S.; Vuluga, D.; Planchat, A.; Legros, J. Hydrogen-bond acceptance of solvents: a ^{19}F solvatomagnetic beta1 database to replace solvatochromic and solvatovibrational scales. *J. Org. Chem.* **2021,** *86*, 4143-4158.